Polar Ionosphere Irregularity Structure and Dynamics by means of X-band Space-borne Synthetic Aperture Radar

Jun Su Kim[a], and Konstantinos Papathanassiou[a]
[a] Microwaves and Radar Institute, German Aerospace Centre, Munchenerstrasse 20 82234 Wessling, Germany

Abstract

The ionosphere effects on microwave propagation and degrades the image quality of space-borne SAR acquisitions. Despite of its reduced effect at high frequencies, phase distortions on the interferograms are often visible on X-band TSX/TDX data. In this paper, the ionospheric phase distortions associated with the small-scale irregularities in TSX/TDX pursuit mode interferograms are analysed. A coincident strong ionospheric drift in the along-track direction is observed by the ground-based high frequency (HF) measurements of SuperDARN. The ionospheric phases are separated from the topographic contributions by using parallax, and the ionospheric altitudes are estimated from the SAR data and cross-validated against SuperDARN data.

1 Introduction

Microwaves propagating through plasma experience a phase advance. In SAR interferometry, the difference of phase advance is demonstrated as characteristic fringes aligned to the geomagnetic field. The isolation and removal of the ionospheric phase contributions on space-borne SAR interferograms using the dispersive nature of the trans-ionospheric propagation have been developed [1].

The high-latitude ionosphere is consistently affected by precipitating charged particles of solar and cosmic origin guided along the geomagnetic field. They form the sheet-shaped ionospheric irregularities [2]. The ionospheric irregularities are flowing nested in the global-scale convection system driven by the $\vec{E} \times \vec{B}$ drift. The convection systems at Arctic and Antarctic are monitored by measuring the Bragg scattering from the irregularities at high frequencies (HF), by means of the Super Dual Auroral network (SuperDARN) [3].

Tandem-X pursuit mode acquisitions enables the along track interferometry (ATI) with a time difference of several seconds. Some TSX/TDX interferograms show clear signs of ionospheric distortions: linear fringes aligned to the geomagnetic field lines. By means of sub-spectral analysis in azimuth direction, the ionospheric phases are separated from other interferometric phase contributions [7], and the altitude and the drift velocity of the irregularities are estimated [9].

2 Ionospheric Irregularity on SAR

2.1 Ionospheric Phase

The phase advance through the ionosphere is proportional to TEC and inversely proportional to the frequency

$$\phi = \frac{4\pi\zeta}{cf} TEC, \tag{1}$$

where $\zeta = \frac{c^2 r_e}{2\pi} = 40.31$ m^3/s^2 r_e is the classical electron radius, c is the speed of light in vacuum and f is the centre frequency. At X-band (f=9.65 GHz), one TECU (=10^{16} m^{-2}) leads to 100° of phase advance.

The long synthetic aperture of SAR system enables the high spatial resolution in azimuth direction. [4] At the same time, the characteristics of the propagation medium may vary. One of the inhomogeneous media is the ionosphere [5]. The rapid, irregular and large change of the ionospheric phase in the synthetic aperture leads to the degradation of the azimuth focusing quality. Ionosphere can change in a rate of a hundred of mTECU/km under severe conditions. This effect is stronger at lower frequencies because the same amount of TEC variation leads to larger phase distortions. In addition, high frequency space-borne SAR has for the same resolution shorter synthetic aperture. The defocusing effect is further suppressed in the shorter synthetic aperture.

The ionospheric phase is detectable only in the interferometric analysis. The interferograms contain contributions from the topography, the troposphere, the ionosphere and any motions of the scatters. For the short temporal baseline of the pursuit TDX mode, the interferometric phase can be interpreted as the superposition of only topographic and ionospheric phase contributions.

2.2 Parallax

During the synthetic aperture, the scatterers are imaged in decreasing squint angles from positive to negative around zero. Different squint angels are associated to different azimuth frequencies. By selecting some part of the azimuth sub-band spectra, the line-of-sight (LOS) and the squint can be restricted, at the cost of azimuth resolution.

As indicated in [6], the ionospheric features change its position in a SAR image along with the squint angle. For

the two approaching and departing azimuth sub-bands, the spectral separation is $W_a/2$, where W_a is the azimuth bandwidth, and the corresponding orbit distance is $B = W_a v_{sat}/2$. Here B stands for the baseline of the parallax in the azimuth direction. Associated with the change of the look-direction, the ionospheric irregularities moves back and forth on SAR image, and the displacement between the two sub-bands D is directly proportional to the ionospheric height h_{iono} as

$$h_{iono} = \frac{D}{B} h_{sat}, \tag{2}$$

where h_{sat} is the satellite height.
Once the displacement D is determined, it is possible to separate the ground contributions and the ionospheric contributions. Any ionospheric phase p at azimuth position x contributes to the sub-band interferograms as

$$\begin{aligned} \phi_{appr}(x) &= g(x) + p(x - \frac{D}{2}) \\ \phi_{depr}(x) &= g(x) + p(x + \frac{D}{2}) \end{aligned} \tag{3}$$

where $g(x)$ is the topographic phase. The shift theorem enables the two contributions p and g to be separated from each other [7]

$$\begin{aligned} \Phi_{appr}(s) &= G(s) + e^{-i\pi Ds} P(s) \\ \Phi_{depr}(s) &= G(s) + e^{i\pi Ds} P(s), \end{aligned} \tag{4}$$

where s is the spatial wavenumber. Subtraction between them leaves only the ionospheric contribution

$$P(s) = \frac{\Phi_{appr}(s) - \Phi_{depr}(s)}{-2i \sin \pi Ds}. \tag{5}$$

One critical problem of this method is the periodicity of the denominator. The noise contribution of the ionospheric phase p does not converge to zero when Ds is any integer. In practice, band-pass filtering should be applied, before $P(s)$ is Fourier transformed back to time domain.

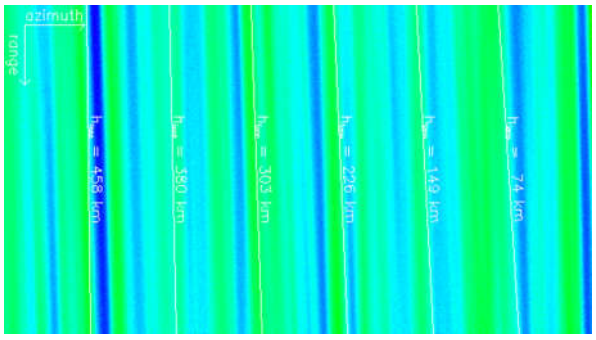

Figure 1 Change of orientation of projected geomagnetic field at different height (annotated) overlaid on the ionospheric phase at X-band (coloured background)

2.3 Orientation

The motion of ions comprising the ionosphere is confined to the geomagnetic field lines, and so do the ionospheric distortions in the SAR images. The direction of the geomagnetic field on the SAR data is discussed in [8] and [9]. The geomagnetic field varies with height, and the range direction extension of the geomagnetic field on the SAR image is proportional to the ionospheric height [9]. This observation allows measuring the ionospheric height by means of the direction of the ionospheric structures. The accuracy of estimating the ionospheric feature alignment directly propagates to the ionospheric altitude estimation.

Figure 1 shows the change of the projected geomagnetic field for different ionospheric altitudes. As the altitude increases, they become more perpendicular to the azimuth direction. From **Figure 1**, it is deducible that the ionospheric altitude is around 300 km where the projection and the phase orientation are most parallel.

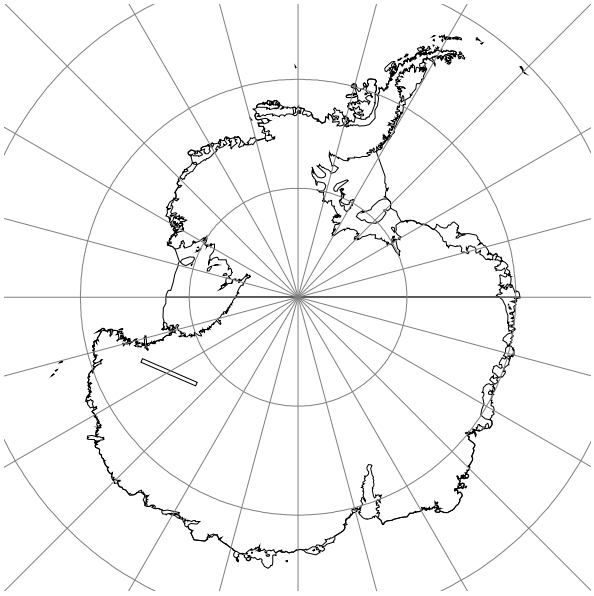

Figure 2 Footprint of TSX/TDX data acquisition (elongated rectangle). The satellite moved from left (east) to right (west).

3 Data/Result/Discussion

3.1 SAR data

In the TSX/TDX pursuit mode interferogram acquired on September 30th, 2014 at 16:30 UT over Antarctica, strong ionospheric irregularities appear. The footprint of the acquisition is shown in **Figure 2**. The orbit is descending, and the scene is acquired from left to right on the map. The scene extent is around 670 km in azimuth and 33 km in range.
Figure 3a (on the last page) shows the corresponding interferogram. Clearly seen are the two kinds of different contributions. The first is the topographic phase which is

prominent at both ends of the scene, and the second is the ionospheric contribution appearing as a "barcode"-pattern in the range direction especially in the middle of the scene. The lack of accurate DEM and unavoidable penetration of microwave into the ice/snow [10], [11] make the perfect compensation of the topographic phase difficult. In order to suppress the topographic contribution, two azimuth sub-band interferograms are generated at approaching and departing sub-bands (positive and negative Doppler bands) and their differentiation is calculated. Because the topographic phases are identical at both sub-bands, the differentiation provides only differentiation of the ionospheric phases [14].

The interferograms at two azimuth sub-bands are shown in **Figure 3b** after band-pass filtering. The filtering is performed in order to emphasise the strongly oriented ionospheric phases, so that their displacement in sub-band images are estimated accurately. The two images are largely similar but the stripes are obviously translated in the azimuth direction of each other. **Figure 3c** shows the estimate of the displacement D defined in Section 2.2. Across the whole scene extent, the displacement remains stable around 800 m. Considering a TSX/TDX orbit altitude of 514 km the ionospheric altitude is estimated to be 200 km.

The ionospheric phase estimated using the methodology of Section 2.2 is shown in **Figure 3d**, as well as, the topographic phase after subtracting the estimated ionospheric phase from the original interferogram is shown in **Figure 3e.** The ionospheric phase is largely compensated, but still there is a remaining periodic undulation. It is partly attributable to the spectral filtering associated to the sinus term in the denominator of (5).

3.2 SuperDARN

Coincident SuperDARN velocity measurements (**Figure 4**) [12] show the ionospheric irregularity and their motion near the SAR data acquisition [13]. Because the map is drawn in geomagnetic coordinate, the grid does not correspond to the one used in **Figure 1**. The ionospheric flow velocity ranges from 250 to 375 m/s, and its direction is aligned in the azimuth direction.

The drift of the irregularities can partly explain the disagreement of the ionospheric heights from the orientation of ionospheric structures in Section 2.3, h_{iono} = 300 km, and form the parallax in Section 3.1, h_{iono} = 200 km. Let us assume the motion of the ionosphere in the azimuth direction during the synthetic aperture time τ. The displacement D on the SAR data is reduced as much as $\frac{\tau}{2} \cdot v_{iono}$, and this modifies the ionospheric altitude estimate as

$$\Delta h_{iono} = \frac{\tau \cdot v_{iono}}{2B} = \frac{v_{iono}}{v_{sat}} h_{sat}. \quad (6)$$

Here the synthetic aperture time is divided by two to represent the time difference between two sub-bands. The ionospheric drift is much slower in comparison to the satellite velocity. In the actual case, the ionospheric drift is about 320 m/s (from the SuperDARN measurement in **Figure 4**) in the azimuth direction reduces the ionospheric height estimation using parallax as much as 21 km. However, the drift alone cannot explain the discrepancy of two ionospheric height estimates.

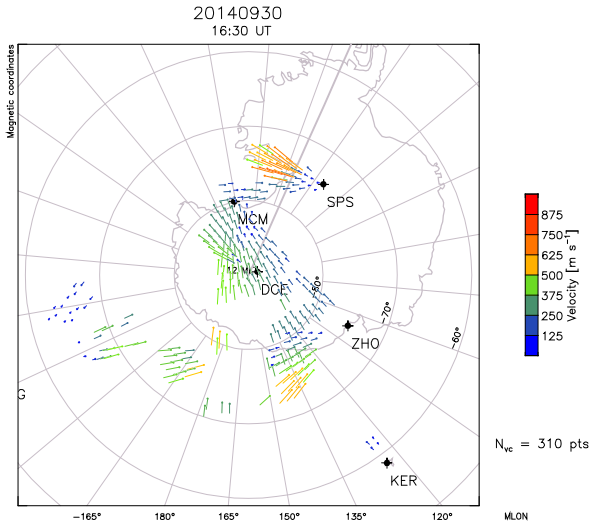

Figure 4 SuperDARN velocity map at the SAR data acquisition time. The map is drawn in geomagnetic coordinate. The speed of ionospheric flow is around 320 m/s near the data footprint. (Accessed through [12])

4 Conclusions

The ionospheric phase found in X-band interferograms over Antarctica is analysed. Strong ionospheric irregularities are detected both in SAR and ground-based radar network. From the azimuth spectral analysis the ionospheric phase could be separated. This approach is different from conventional split spectrum method relying on dispersion, and sensitive to much smaller scale ionospheric structures. At the same time, this method inherently bears a blind point in the spectra that leaves small but periodic artefacts on the corrected interfrogram.

The ionospheric altitudes were estimated by means of parallax and the orientation of ionospheric features. The two estimates show rather large discrepancy of 100 km. The SuperDARN velocity measurement shows fast ionospheric flow of around 320 m/s in speed in the azimuth direction across the SAR data footprint. The effect of the drift on the altitude estimation using parallax is analysed, but it cannot explain completely the observed difference of the ionospheric height estimates.

5 Literature

[1] Gomba, G. et al., Toward Operational Compensation of Ionospheric Effects in SAR Interferograms: The Split-Spectrum Method, *IEEE Trans. Geosci. Remote Sens.*, Vol. 54, No. 3, Mar. 2016, pp. 1446-1461

[2] Aaron, J., Global morphology of ionospheric scintillation, *Proc. IEEE*, Vol. 70, No. 4, 1982, pp. 360-378

[3] Chisham, G. et al., A decade of the Super Dual Auroral Radar Network (SuperDARN): scientific achievements, new techniques and future directions, *Surv. Geophys.*, Vol. 28, 2007, pp.33-109

[4] Curlander J. and McDonough R., Synthetic Aperture Radar: Systems and Signal Processing, Wiley, 1991

[5] Kim, J. et al., Correcting Distortion of Polarimetric SAR data Induced by Ionospheric Scintillation, *IEEE Trans. Geosci. Remote Sens.*, Vol. 53, No. 12, Dec. 2015, pp. 6319-6335

[6] Kim, J and Papathanassiou, K, SAR Observation of Ionosphere Using Range/Azimuth Sub-bands, EUSAR, June 2014, Berlin (Germany)

[7] Kim, J and Papathanassiou, K, On the Separation of Dynamic Scattering and Ionospheric Effects in SAR Data, POLinSAR, January 2015, Frascati (Italy)

[8] Meyer at al., The Influence of Equatorial Scintillation on L-Band SAR Image Quality and Phase, *IEEE Trans. Geosci. Remote Sens.*, Vol. 54, No. 2, Feb. 2016, pp. 869-88

[9] Kim, J., et al., Detection and Estimation of Equatorial Spread F Scintillations using Synthetic Aperture Radar, *IEEE Trans. Geosci. Remote Sens.*, Vol. 55, No. 12, Dec. 2017, pp. 6713-6725

[10] Rizzoli, P., et al. Characterization of Snow Facies on the Greenland Ice Sheet Observed by TanDEM-X Interferometric SAR Data, *Remote Sens.*, Vol. 9, No. 4, Mar. 2017, p. 315

[11] Fischer, G., Papathanassiou, K., and Hajnsek, I., Modeling and Compensation of the Penetration Bias in InSAR DEMs of Ice Sheets at Different Frequencies, (submitted) *IEEE J. Sel. Topics Appl. Earth Observ. Remote Sens.*

[12] Center for Space Science and Engineering Research, Virginia Polytechnic Institute and State University, http://vt.superdarn.org/tiki-index.php?page=Map+Velocity+Tool

[13] Mohanty, S, Carrano, C. S., and Singh, G., Effect of Anisotropy on Ionospheric Scintillations Observed by SAR, *IEEE Trans. Geosci. Remote Sens.*, Vol. 57, No. 9, Sep. 2019, pp. 6888-6899

[14] Prats, P. et al, Comparison of Topography- and Aperture-Dependent Motion Compensation Algorithms for Airborne SAR, *IEEE Geosci. Remote Sens. Lett.*, Vol. 4, No. 3, Jul. 2007, pp. 349-353

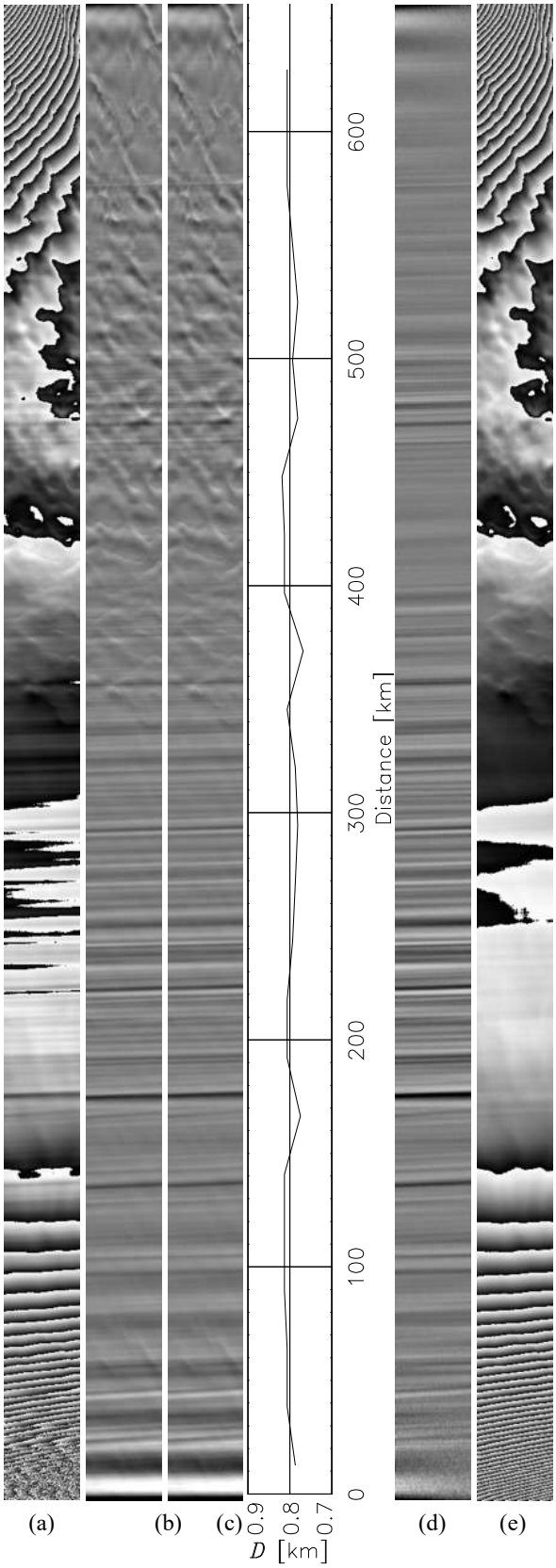

Figure 3 Interferograms. (a) original interferogram. (b) band-passed approaching and departing interferograms. (c) Relative shift estimates (d) estimated ionospheric phase (e) residual topographic phase